nanomaterials

Article

Effects of Synthesis Conditions of $Na_{0.44}MnO_2$ Precursor on the Electrochemical Performance of Reduced Li_2MnO_3 Cathode Materials for Lithium-Ion Batteries

Ya Sun [1],*, Jialuo Cheng [1], Zhiqi Tu [1], Meihe Chen [1], Qiaoyang Huang [2], Chunlei Wang [1] and Juntao Yan [1],*

[1] College of Chemistry and Environmental Engineering, Wuhan Polytechnic University, Wuhan 430023, China; 13995967507@163.com (J.C.); tzq061721@163.com (Z.T.); 15327194236@163.com (M.C.); wangcl@whpu.edu.cn (C.W.)
[2] School of Textile Science and Engineering, Wuhan Textile University, Wuhan 430200, China; 13986938081@163.com
* Correspondence: sunya230@whpu.edu.cn (Y.S.); 12111@whpu.edu.cn (J.Y.)

Abstract: Li_2MnO_3 nanobelts have been synthesized via the molten salt method that used the $Na_{0.44}MnO_2$ nanobelts as both the manganese source and precursor template in $LiNO_3$-LiCl eutectic molten salt. The electrochemical properties of Li_2MnO_3 reduced via a low-temperature reduction process as cathode materials for lithium-ion batteries have been measured and compared. Particularly investigated in this work are the effects of the synthesis conditions, such as reaction temperature, molten salt contents, and reaction time on the morphology and particle size of the synthesized $Na_{0.44}MnO_2$ precursor. Through repeated synthesis characterizations of the $Na_{0.44}MnO_2$ precursor, and comparing the electrochemical properties of the reduced Li_2MnO_3 nanobelts, the optimum conditions for the best electrochemical performance of the reduced Li_2MnO_3 are determined to be a molten salt reaction temperature of 850 °C and a molten salt amount of 25 g. When charge–discharged at 0.1 C (1 C = 200 mAh g^{-1}) with a voltage window between 2.0 and 4.8 V, the reduced Li_2MnO_3 synthesized with reaction temperature of $Na_{0.44}MnO_2$ precursor at 850 °C and molten salt amounts of 25 g exhibits the best rate performance and cycling performance. This work develops a new strategy to prepare manganese-based cathode materials with special morphology.

Keywords: $Na_{0.44}MnO_2$; Li_2MnO_3; nanobelts; molten-salt method; rate performance; cathode material

check for updates

Citation: Sun, Y.; Cheng, J.; Tu, Z.; Chen, M.; Huang, Q.; Wang, C.; Yan, J. Effects of Synthesis Conditions of $Na_{0.44}MnO_2$ Precursor on the Electrochemical Performance of Reduced Li_2MnO_3 Cathode Materials for Lithium-Ion Batteries. *Nanomaterials* **2024**, *14*, 17. https://doi.org/10.3390/nano14010017

Academic Editor: Carlos Miguel Costa

Received: 19 November 2023
Revised: 13 December 2023
Accepted: 17 December 2023
Published: 20 December 2023

1. Introduction

As the energy crisis and environmental degradation are intensifying, countries around the world have made carbon reduction commitments to achieve carbon neutrality [1,2]. Developing new energy, realizing energy transformation, and building a green and low-carbon energy system are important measures to reduce carbon dioxide emissions and achieve global carbon neutrality. Lithium-ion batteries (LIBs) stand out in the fields of energy storage devices (electric vehicles, hybrid electric vehicles) and intermittent renewable energy storage because of their high energy density, low cost, and stable cycle life [3–8]. As a critical member of LIBs, cathode materials play an important role in the electrochemical performance of LIBs [9–11]. Among the potential cathodes, Li-rich layered oxide has been under intense investigation because of its low cost, low toxicity, high specific capacity, and high energy density [12–14].

As the terminal member of LLO materials, Li_2MnO_3 has been an ideal cathode candidate with a theoretical specific capacity of 459 mAh g^{-1}, rich Mn resource, and low cost [15,16]. However, different from other Mn-based cathode materials, the valence of Mn in Li_2MnO_3 is +4 and cannot be further oxidized, resulting in no electrochemical activity in the common voltage range (2.0~4.4 V) [17,18]. It is usually electrochemically activated at a high cut-off voltage (4.8 V) during the initial charging process, which results in serious capacity and voltage decay [19,20]. Consequently, other strategies have been proposed to activate or enhance the electrochemical properties of Li_2MnO_3. One is to partially replace Li, Mn, and O with other elements [21–23]. Chen et al. [21,22] explored the influence of the substitution of Nb and Mo on the electrochemical performance of Li_2MnO_3. The results showed that the improved electrochemical properties were attributed to the additional electronic compensation provided by Nb^{5+} and Mo^{3+} for Li_2MnO_3, and retarded the release of oxygen during discharging process. The spinel phase $LiMn_2O_4$ was introduced into Li_2MnO_3 to form a layered-spinel integrated composite by Wu and He et al. [24,25], exhibiting extremely high specific capacity and excellent high-rate performance. Li_2MnO_3 in the integrated structure improves the high specific capacity, while $LiMn_2O_4$ provides a three-dimensional lithium-ion transport channel for the composite, thus enhancing the ratability [24–26]. Moreover, the chemical thermal reduction method is also utilized to propose the outstanding electrochemical properties of layered lithium-rich cathodes [26–29].

Particle size reduction or controlled special morphology has been an effective strategy to improve the electrochemical performance of Li-rich materials [30–33]. Particle size reduction can reduce the diffusion distance of lithium ion, and nanostructured materials have unique structural which can provide a favorable one-dimensional electron pathway [34].

$Na_{0.44}MnO_2$ with nanoribbons and nanowires has been used as both the Na source and precursor to prepare lithium–manganese oxides with the corresponding morphology [35,36]. The molten salt method can realize the preparation of anisotropic powder materials with specific components at low reaction temperatures or in a short time as a method of synthesizing inorganic compounds [37,38]. The structure of the obtained materials is relatively uniform with no or only weak agglomeration, and nanomaterials with specific morphology can be synthesized by adjusting the reaction conditions. The factors affecting the morphology of the materials prepared via the molten salt method mainly include the type and amount of salt, reaction temperature, and reaction time, etc. [39]. Zhang et al. [40] synthesized Li_2MnO_3 nanoribbons via the precursor template $Na_{0.44}MnO_2$ nanoribbons with the mixture of $LiNO_3$-LiCl as molten salt, and studied the magnetic behaviors. Our previous works have proven that Li_2MnO_3 nanobelts/nanowires can be successfully prepared using a $Na_{0.44}MnO_2$ precursor, and the low-temperature reduction products exhibit improved electrochemical performance [27–29]. However, the relationships between the synthesis conditions of a $Na_{0.44}MnO_2$ precursor and the electrochemical performances of reduced Li_2MnO_3 could be further discussed.

Here, the $Na_{0.44}MnO_2$ nanobelt precursor was fabricated via the molten salt method, and then the precursor was lithiated to obtain Li_2MnO_3 nanobelts. The influences of reaction temperature and molten salt contents on the crystallinity and morphology of $Na_{0.44}MnO_2$ precursor, as well as on the electrochemical performance of low-temperature-reduced products were also discussed. In addition, the growth mechanism of $Na_{0.44}MnO_2$ nanobelt precursor was investigated by adjusting the reaction time.

2. Experimental

2.1. Material Synthesis

Synthesis of $Na_{0.44}MnO_2$ nanobelts: Analytical NaCl was used as molten salts without further treatment. Na_2CO_3 and $MnCO_3$ were fully ground with a certain amount of NaCl in an agate mortar according to the stoichiometric ratio; then, the ground powders were transferred to the crucible. The mixture reacted in a muffle furnace at 800–900 °C for a certain time. After cooling to room temperature, the calcined product was filtered, washed with a large amount of deionized water, and dried at 100 °C.

Synthesis of Li_2MnO_3 nanobelts: Analytical $LiNO_3$ and LiCl mixture were used as molten salts without further treatment. At the same time, $LiNO_3$ was used as the oxidizing reagent. $Na_{0.44}MnO_2$ precursor was fully ground with 88 mol% $LiNO_3$ and 12 mol% LiCl in an agate mortar, then transferred to the crucible. The mixture was sintered at 500 °C for 1 h. After cooling to room temperature, the sintered product was washed with a large amount of deionized water, and dried at 100 °C. In this process, Li_2MnO_3 involved the ion exchange between Li^+ in molten $LiNO_3$ and LiCl salts and Na^+ in $Na_{0.44}MnO_2$ and the oxidation process by $LiNO_3$ according to previous work [40].

Low-temperature reduction of Li_2MnO_3 nanobelts: The reduced Li_2MnO_3 nanobelts were synthesized according to our previous work [27–29]. The prepared Li_2MnO_3 nanobelts, stearic acid, and an appropriate amount of absolute ethanol were ground for a few minutes to obtain a uniform solid–liquid rheological material. Then, the obtained rheological material was heated at 340 °C in an Ar atmosphere for 8 h. After washing several times, the product was obtained. The mol ratio of Li_2MnO_3 nanobelts and stearic acid was 1:0.04.

2.2. Materials Characterization

The crystal structures of the as-prepared samples were conducted on a Bruker D8 ADVANCE (Berlin, Germany) X-ray diffraction via Cu-Kα radiation. The as-prepared $Na_{0.44}MnO_2$ samples were operated over a 2θ range of 5–60° at rates of 5°/min; Li_2MnO_3 and low-temperature reduction of Li_2MnO_3 were operated over a 2θ range of 10–80° at rates of 5°/min. The morphology of the as-synthesized samples was characterized using scanning electron microscopy (SEM, FEI, SIRION, Eindhoven, The Netherlands) with a working voltage of 20 kV.

2.3. Electrochemical Tests

To fabricate the electrodes, the as-synthesized samples were mixed with super P and polytetrafluoroethylene (PTFE) at a ratio of 80:15:5 onto Al foil. In an Ar-filled glovebox, the batteries were assembled using lithium foil, Celgard 2300 microporous films, 1 M $LiPF_6$ in the ethylene carbonate (EC), and dimethyl carbonate (DMC) (1:1 *v*/*v*) as anodes, separators, and electrolytes, respectively. The electrochemical tests were performed on a Neware battery test system (Shenzhen, China) at a voltage window between 2.0 and 4.8 V, ranging from 0.1 C to 5 C.

3. Results and Discussion

3.1. Effects of Molten Salt Reaction Temperature

In chemical reactions, temperature has a great influence on reaction rates. At higher temperatures, the motion rate of molecules or ions can be accelerated, and the average kinetic energy and the collision frequency of molecules will accelerate in unit time. Therefore, the temperature of the synthesis process plays a vital role in the crystallinity of products [41].

Figure 1 shows the XRD patterns of $Na_{0.44}MnO_2$ synthesized at 800, 850, and 900 °C (denoted as NMO-800, NMO-850, and NMO-900) via the molten salt method. It can be seen from the figure that the main phase of the samples prepared at different temperatures is the characteristic peak of orthogonal phase $Na_4Mn_9O_{18}$ (JCDS. No. 27-0750) [40], and the $Na_{0.91}MnO_2$ impurity phase appears in the samples. With the increase in reaction temperature, the characteristic peaks of $Na_{0.44}MnO_2$ are continuously enhanced and the crystallinity becomes stronger.

SEM images of $Na_{0.44}MnO_2$ precursor synthesized at different temperatures are shown in Figure 2. The as-prepared samples all exhibit the nanobelts' morphology with lengths of one to several tens of micros, and with a width that varies with different temperatures. When the reaction temperature is 800 °C, the average width of $Na_{0.44}MnO_2$ nanobelts is about 200 nm, and a small number of nanosheets appear in the sample, while the average width is about 240 nm with a reaction temperature of 850 °C. When the temperature rises to 900 °C, the average width of nanobelts is about 250 nm with particles agglomerated. As the reaction temperature increased from 800 to 900 °C, the average width of the samples increased, which is mainly because the increased reaction temperature promotes the growth of the crystal. Additionally, the increase in temperature may lead to an increase in heating time and cooling, which is equivalent to prolonging the reaction time and accelerating the growth of the sample. In general, the suitable temperature of $Na_{0.44}MnO_2$ is 850 °C because the $Na_{0.44}MnO_2$ nanobelts synthesized at that temperature are the most uniform and have no agglomeration.

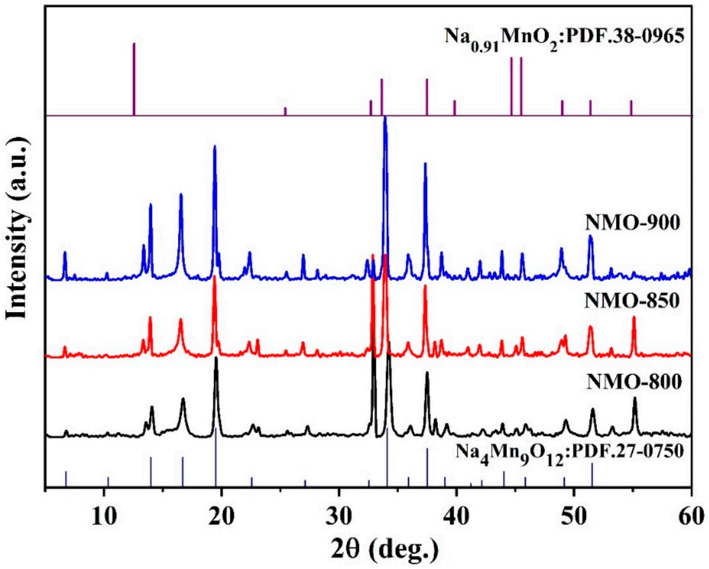

Figure 1. The XRD patterns of NMO-800, NMO-850 and NMO-900.

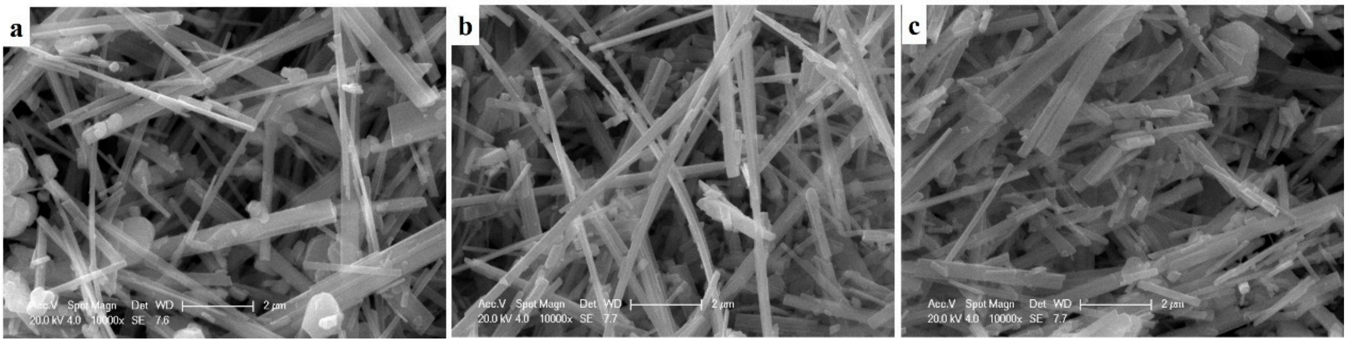

Figure 2. SEM images of NMO-800 (**a**), NMO-850 (**b**) and NMO-900 (**c**).

From Figure 3, it is obvious that both Li_2MnO_3 (marked as LMO-800, LMO-850, and LMO-900) and the reduced R-Li_2MnO_3 (denoted as R-LMO-800, R-LMO-850, and R-LMO-900) show sharp peaks and flat bases, indicating that the synthesized samples have high crystallinity. All XRD diffraction peaks, which can be seen from Figure 3a, are indexed to the monoclinic phase Li_2MnO_3 with a space group of C2/m [42]. The feature of the XRD pattern is the superstructure in a range of 20~25°, which is related to the ordered arrangement of Li/Mn in the transition metal layer. After reduction, the diffraction peaks of these superstructures still exist in the samples with weak intensity, suggesting that the low-temperature reduction process has a certain effect on the superstructure. It is worth noting that the intensity of diffraction peaks also increases with increasing temperature. In addition, several new peaks appear in Figure 3b, such as at 15.5° and 61.3°, which were ascribed to the (010) and (221) planes of orthorhombic $LiMnO_2$.

SEM images of Li_2MnO_3 nanobelts and the reduced R-Li_2MnO_3 nanobelts are displayed in Figure 4. It can be clearly seen that Li_2MnO_3 still maintains the morphology of the $Na_{0.44}MnO_2$ nanobelt precursor, with a length of one to several microns. The average width of LMO-800 is about 150 nm, while the LMO-850 is 190 nm and LMO-900 is 220 nm. Among the three materials, LMO-850 has the most uniform particle size and the smallest width. After the lithiation of $Na_{0.44}MnO_2$, the length and width of the material decrease, and the surface of material becomes rough, which is mainly due to the transition from the tunnel structure of $Na_{0.44}MnO_2$ to the layered structure of Li_2MnO_3. Figure 4d–f shows a series of samples of Li_2MnO_3 after low-temperature reduction. After reduction, the samples are still nanobelts, demonstrating that the low-temperature reduction process has no effect on the morphology. However, the length of the material is shorter than that before reduction, and some layered structures are broken. The average width of R-LMO-800 is 170 nm, the average width of R-LMO-850 is 180 nm, and the average width of R-LMO-900 is 190 nm. The particle size of cathodes affects electrochemical properties; therefore, the three samples will exhibit different electrochemical performance.

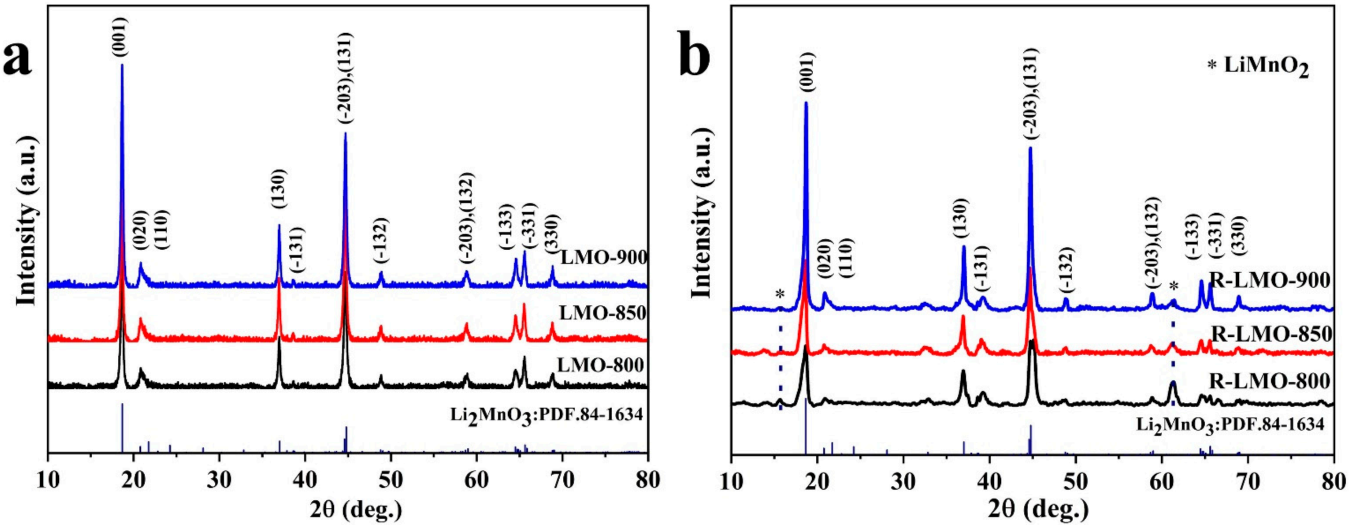

Figure 3. XRD patterns of Li_2MnO_3 nanobelts (**a**) and the reduced R-Li_2MnO_3 nanobelts at different temperatures (**b**).

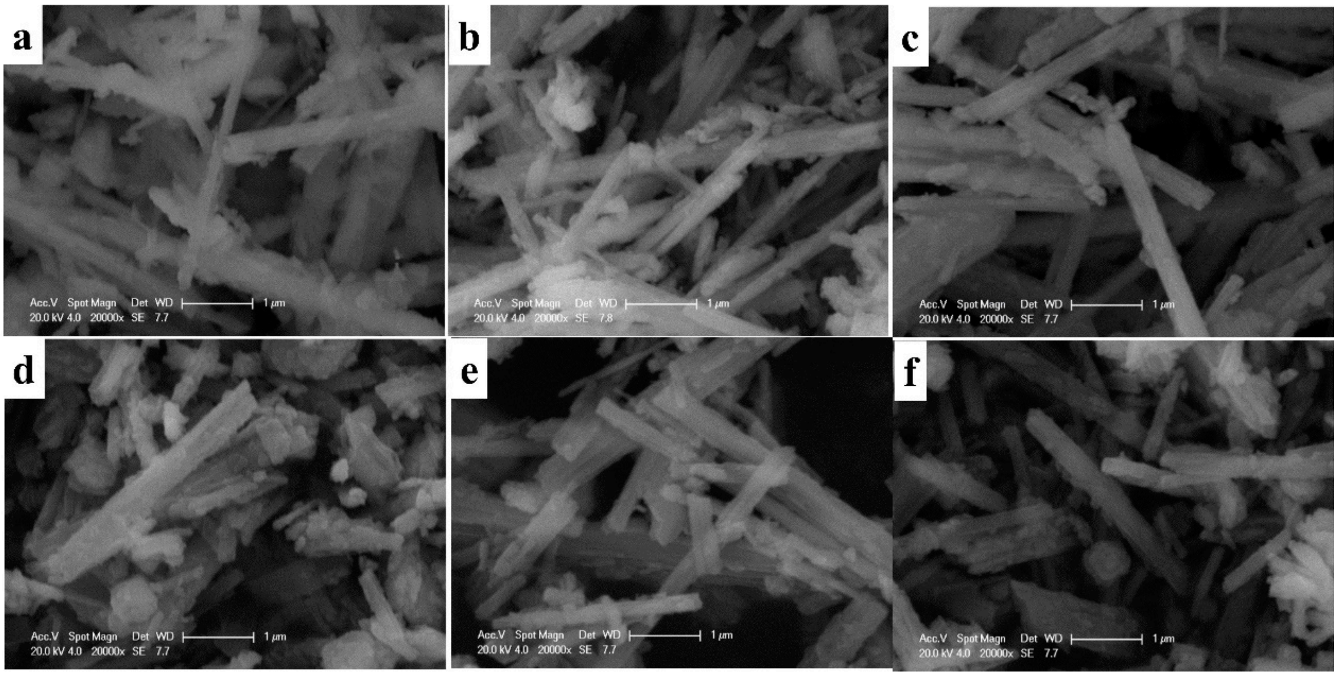

Figure 4. SEM images of Li_2MnO_3 nanobelts, (**a**) LMO-800, (**b**) LMO-850 and (**c**) LMO-900, and the reduced R-Li_2MnO_3 nanobelts, (**d**) R-LMO-800, (**e**) R-LMO-850 and (**f**) R-LMO-900.

To investigate the influence of the synthesis temperature of the precursor on the final products, galvanostatic charging–discharging tests were performed at room temperature.

Figure 5a,b exhibits the initial classical charging–discharge curves and the corresponding cycle performance of three reduced samples under the voltage window of 2.0~4.8 V at 0.1 C (1 C = 200 mAh g^{-1}). From Figure 5a,b, it can be seen that the initial discharge-specific capacities of R-LMO-800, R-LMO-850, and R-LNO-900 can reach 154.5, 162.4, and 185.3 mAh g^{-1}, respectively. After 100 cycles, the discharge-specific capacities of the three samples are 140.3, 158.3, and 147.4 mAh g^{-1}, with corresponding capacity retention rates of 90.8%, 97.4%, and 79.6%, respectively. Additionally, the curves of the three reduced samples are quite different from pristine Li_2MnO_3, which has been confirmed in our previous works [27–29]. The rate performance of three samples at rates of 0.1 C, 0.5 C, 1 C, 2 C, and 5 C with each rate cycling for 20 cycles is shown in Figure 5c. It is clearly shown that the ratability of R-LMO-850 is better than that of the other two samples at various rates. However, at high rates of 2 C and 5 C, the performance of R-LMO-800 and R-LMO-900 is quite similar. The discharge-specific capacities of RLMO-850 at 0.5 C, 1 C, 2 C, and 5C are 136.4, 121.1, 106.6, and 82.5 mAh g^{-1}, respectively.

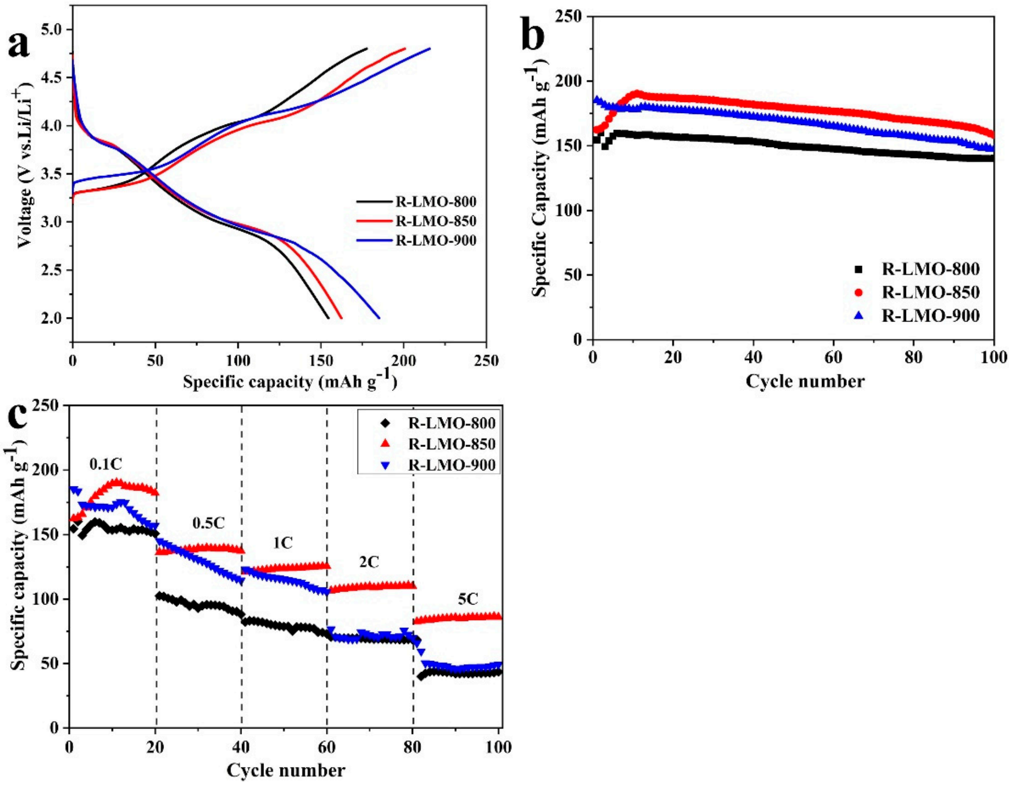

Figure 5. The classical initial charging–discharging curves (**a**), the corresponding cycle performance (**b**) of R-LMO-800, R-LMO-850 and R-LMO-900 at 0.1 C rate, and the rate performance at different rates (**c**).

Obviously, the cyclability and ratability of R-LMO-850 are the best when the reaction temperature of the $Na_{0.44}MnO_2$ precursor is 850 °C. Nevertheless, the initial discharge-specific capacity of R-LMO-850 is slightly lower than that of R-LMO-900. From the XRD patterns and SEM images of the low-temperature-reduced samples, it can be seen that the crystallinities are becoming higher with the increase in reaction temperature. Some studies reported that higher crystallinity could promote the transport of lithium ion since higher crystallinity indicated fewer defects and stacking faults [43]. Moreover, smaller particles can reduce the polarization of electrodes during the charging–discharging process, and then improve the specific capacity. The uniformly disturbed particles can effectively utilize each particle, increase the discharge depth, and finally enhance the electrochemical performance [44,45]. R-LMO-850 nanobelts show smaller sizes than those of R-LMO-900. With the uniformed particle and small particle size, R-LMO-850 effectively utilizes each particle, and shortens the diffusion distance of lithium ions during the charge and discharge process, along with the best performance. Meanwhile, R-LMO-850 exhibits better crystallinity than R-LMO-800, resulting in better electrochemical capacities than R-LMO-800.

3.2. Effects of Molten Salt Contents

Figure 6 displays the XRD patterns of the $Na_{0.44}MnO_2$ precursor synthesized with different molten salt contents (denoted as NMO-20, NMO-25, and NMO-30). All samples correspond to the orthorhombic phase of $Na_4Mn_9O_{18}$ with a space group of *Pbam*. The intensities of the diffraction peaks have no obvious differences with changes in the amounts of molten salt, which indicates that the molten salt contents in the reaction process make no difference in the crystallinity of materials. At the same time, the reflection peaks of all the samples are obvious and sharp with good crystallinity.

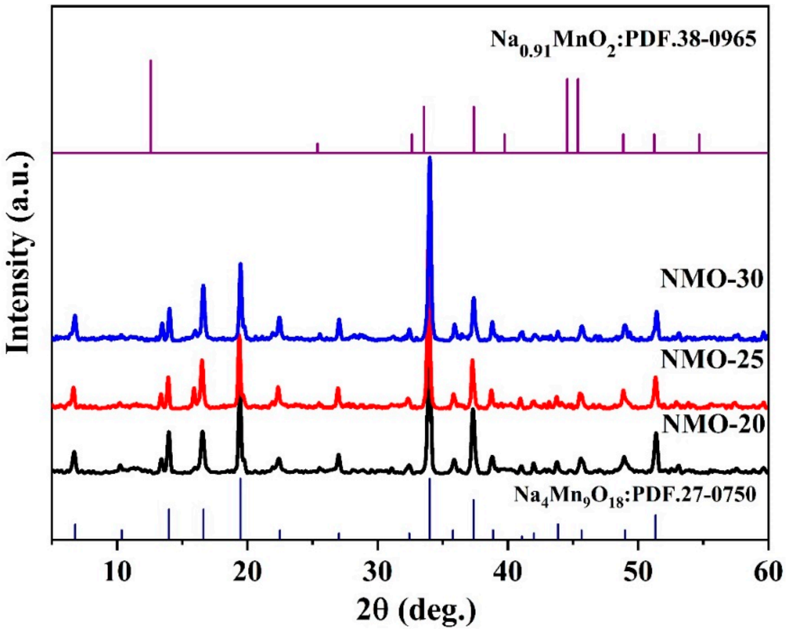

Figure 6. XRD patterns of $Na_{0.44}MnO_2$ precursor synthesized with different molten salt content.

SEM images and the corresponding particle size distribution of the $Na_{0.44}MnO_2$ precursor synthesized with different molten salt content are shown in Figure 7. It is obvious that all the samples are nanobelts with a length of one to several tens of microns. The change in molten salt content has little effect on the length of the samples; however, it is quite different for the width. According to figures of particle size distribution, the average widths of NMO-20, NMO-25, and NMO-30 are 240, 207, and 280 nm, respectively, with relatively wide particle size distribution. Moreover, NMO-25 exhibits the smallest particle size.

A series of Li_2MnO_3 samples were obtained via lithiation of $Na_{0.44}MnO_2$ precursors synthesized using different amounts of molten salt, which were labeled LMO-20, LMO-25, and LMO-30, respectively. Then, the lithiated samples were reduced at low temperatures to obtain the final products, marked as R-LMO-20, R-LMO-25 and R-LMO-30, respectively. The corresponding XRD patterns are shown in Figure 8. It can be seen that the samples after lithiation and the final products after low-temperature reduction can be assigned to monoclinic Li_2MnO_3 (PDF. 86-1634) with a space group of C2/m. The reflection peaks of all the samples are sharp, suggesting that the crystallinity of the samples is good. Additionally, there is little effect on the crystallinity of all the samples with different amounts of molten salt. After low-temperature reduction, the diffraction peaks at 15.5° and 61.3°, which can be assigned to the (010) and (221) planes of orthorhombic $LiMnO_{2,}$ appear in the pattern.

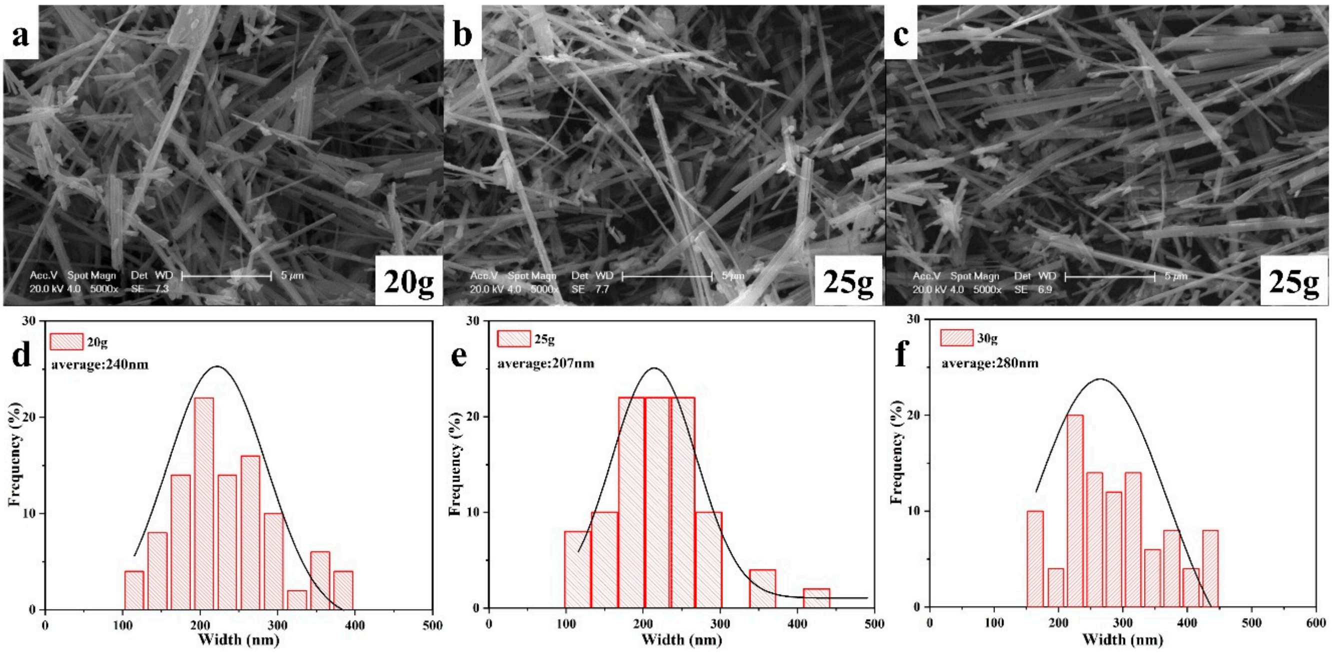

Figure 7. SEM images and size distributions of NMO-20 (**a**,**d**), NMO-25 (**b**,**e**), and NMO-30 (**c**,**f**).

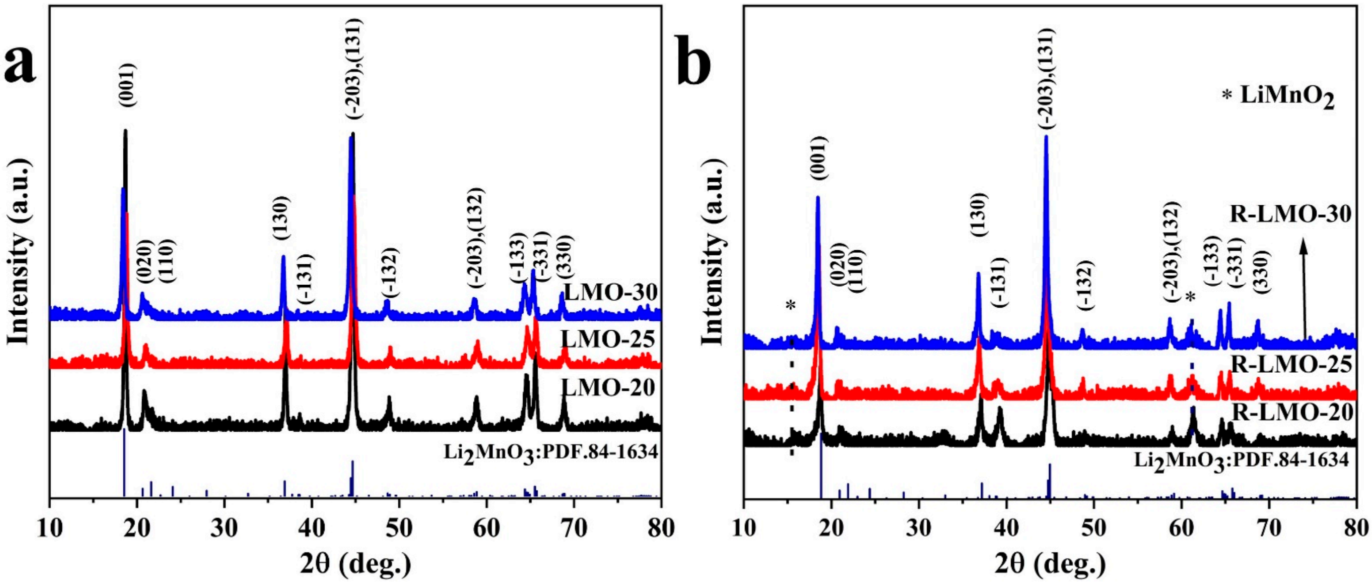

Figure 8. XRD patterns of Li_2MnO_3 nanobelts (**a**) and the reduced R-Li_2MnO_3 nanobelts with different molten salt content (**b**).

Figure 9a–c exhibits SEM images of Li_2MnO_3 synthesized via $Na_{0.44}MnO_2$ with different molten salt contents. As can be seen, the lithiation process has no influence on the morphology of materials. Li_2MnO_3 still retains the morphology of nanobelts with decreased length. The average particle sizes of LMO-20, LMO-25, and LMO-30 are 250, 210, and 280 nm, respectively. LMO-25 has the smallest particle size and a relatively uniform distribution. After low-temperature reduction, the samples also maintain the nanobelts' morphology, indicating undamaged morphology during the reduction process. R-LMO-20, R-LMO-25, and R-LMO-30 show particle sizes of 240, 220, and 260 nm, respectively.

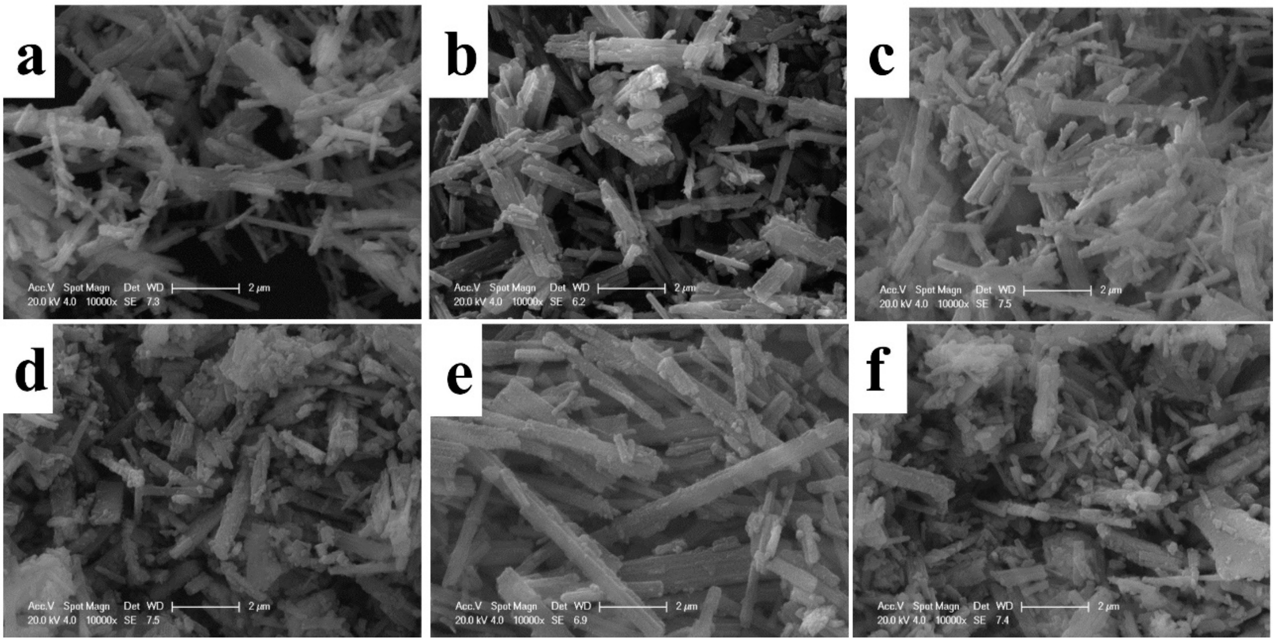

Figure 9. SEM images of Li_2MnO_3 synthesized via $Na_{0.44}MnO_2$ with different molten salt contents: (**a**) LMO-20, (**b**) LMO-25, (**c**) LMO-30 and reduced R-Li_2MnO_3: (**d**) R-LMO-20, (**e**) R-LMO-25, and (**f**) R-LMO-30.

Figure 10a,b presents the initial charging–discharging curves of R-LMO-5, R-LMO-20, R-LMO-25, and R-LMO-30 and the corresponding 30 cycles' performance at 0.1 C. The specific discharge capacities of R-LMO-20, R-LMO-25, and R-LMO-30 in the first cycle are 132.6, 176.8, and 163.8, respectively. After cycling for 100 cycles, the specific discharge capacities of all the samples undergo a process of rising and then falling. In the 100th cycle, the specific discharge capacities are 90.7, 154.2, and 145.3 mAh g^{-1}, respectively. The rate performance of all the samples cycled for 10 cycles at rates varying from 0.1 C to 5 C is shown in Figure 10c. Note that R-LMO-25 possesses the best performance at various rates, R-LMO-20 is the second, and R-LMO-20 is the worst. It can be concluded that when the amount of molten salt in the reaction system is 25 g, the specific capacity, cycle performance, and ratability of the final product are the best because R-LMO-25 has the smallest particle size and the most relatively uniform particles among the three samples.

3.3. Growth Mechanism of $Na_{0.44}MnO_2$ Nanobelts

In order to study the growth mechanism of $Na_{0.44}MnO_2$ nanobelts, the reaction temperature was controlled at 850 °C, and the molten salt content was 5 g; the XRD and SEM images of different reaction times are shown in Figure 11. At the initial stage of reaction, that is, when the reaction time is 60 s, it can be seen from the XRD pattern that the main phase of the product is $Na_{0.91}MnO_2$, and there are also fewer characteristic peaks of $Na_{0.44}MnO_2$. It is reported that in the process of synthesizing tunnel-structured sodium manganese compounds, $Na_{0.91}Mn0_2$ usually appears as the intermediate phase or precursor with a layered structure [46,47]. From the corresponding SEM images, it can be found that the products are mainly nanosheets and there are very few nanobelts, indicating that the nanosheets and nanobelts may be $Na_{0.91}MnO_2$ and $Na_{0.44}MnO_2$, respectively. The intensities of $Na_{0.91}MnO_2$ peaks weaken, while those of $Na_{0.44}MnO_2$ peaks enhance upon increasing the reaction time to 10 min. Most of the products are nanosheets, with a small number of nanobelts. With the reaction time increasing to 30 min and 60 min, the characteristic peak of $Na_{0.44}MnO_2$ in the product is continuously enhanced with the morphology of nanobelts. At last, when the reaction time is 5 h, the product is completely $Na_{0.44}MnO_2$.

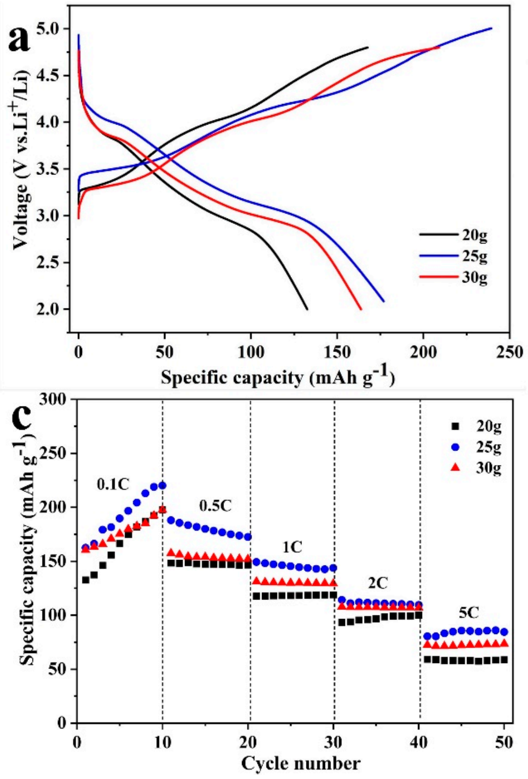

Figure 10. The classical initial charging–discharging curves (**a**), the corresponding cycle performance (**b**) of R-LMO-20, R-LMO-25 and R-LMO-30 at 0.1 C rate, and the rate performance at different rates (**c**).

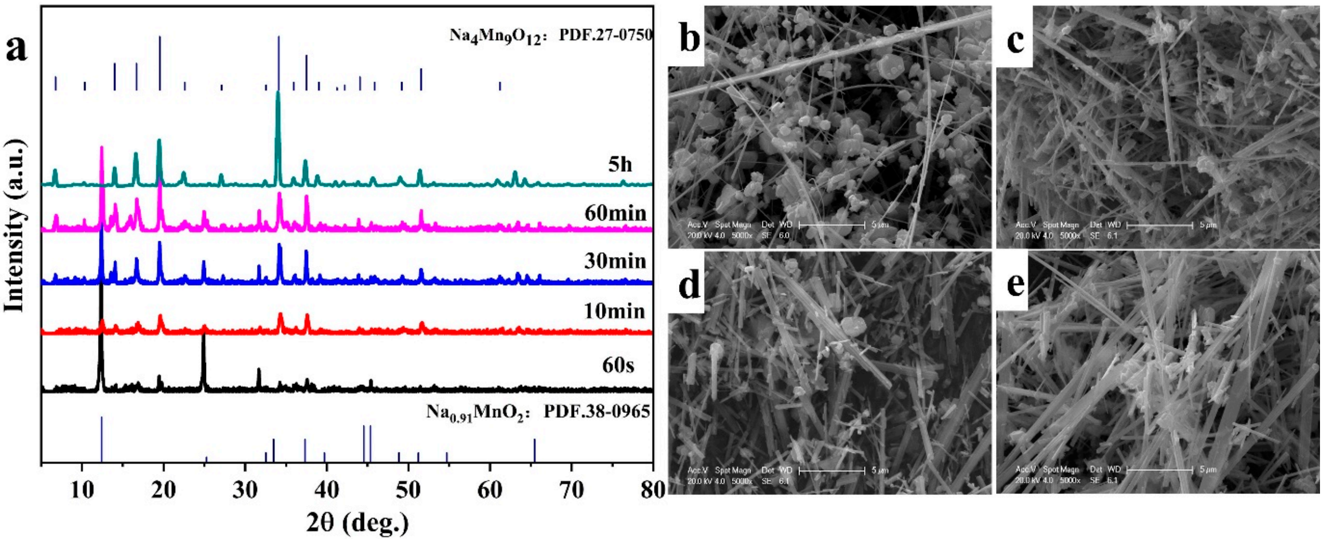

Figure 11. XRD patterns of $Na_{0.44}MnO_2$ at different reaction time (**a**) and SEM images of reaction for 60 s (**b**), 10 min (**c**), 30 min (**d**), and 60 min (**e**).

Recently, there have been many reports on the growth mechanism of special morphologies. Li et al. [48] studied the hydrothermal preparation of $Na_{0.5}MnO_2$ nanowires, in which Na-Birnessite was the intermediate phase. In this work, nanowires were formed through the fracture of nanosheets. Wang et al. [47] investigated the growth mechanism of MnO_2 nanowires by combining the results of XRD and TEM, indicating that nanowires were formed by crimping nanosheets. However, in the process of synthesizing $Na_{0.44}MnO_2$ nanobelts, no signs of the breakage of nanosheets were found. Therefore, it could be speculated that $Na_{0.44}MnO_2$ nanobelts were formed by crimping $Na_{0.91}MnO_2$ nanosheets. Moreover, $Na_{0.44}MnO_2$ may be grown according to the Ostwald ripening mechanism, that is, a crystal growth model in which large particles grow and small particles dissolve [49,50]. In the process of synthesizing $Na_{0.44}MnO_2$ nanobelts, the possible reactions are as follows:

$$\text{fast}: \ MnCO_3 + Na_2CO_3 + O_2 \rightarrow Na_{0.44}MnO_2 + CO_2 \tag{1}$$

$$\text{slow}: \ MnCO_3 + NaCl + O_2 \rightarrow Na_{0.44}MnO_2 + Cl_2 \tag{2}$$

The first step is very quick as it can usually be completed in a few minutes, while the second step is completed in a few hours. At the beginning of the reaction, when the amount of $MnCO_3$ is sufficient, the first step of the reaction occurs, which explains that the $Na_{0.44}MnO_2$ phase appears in the system when the reaction time is 60 s. As the time increases to 60 min, small particles grow into nanosheets, some nanobelts develop, and some nanosheets curl into nanobelts. When the reaction reaches 1 h, the Na_2CO_3 reaction is completed, and the second step of the reaction occurs. At this time, the $Na_{0.91}MnO_2$ phase gradually disappears, and the reaction process is slow and lasts for a long time.

As shown in Figure 12, the formation process of a $Na_{0.44}MnO_2$ nanobelt can be summarized as follows: Firstly, the $Na_{0.91}MnO_2$ nanosheet with a layered structure is formed rapidly through the reaction. This process may be that sodium ion is dissolved in $MnCO_3$ particles, structural transformation occurs at the same time, and there is a small amount of nanobelts in the reaction; then, the nanosheet curls to form a nanostrip, together with the transition from the layered structure to the tunnel structure at the same time, and the nano strip grows according to the Ostwald ripening mechanism.

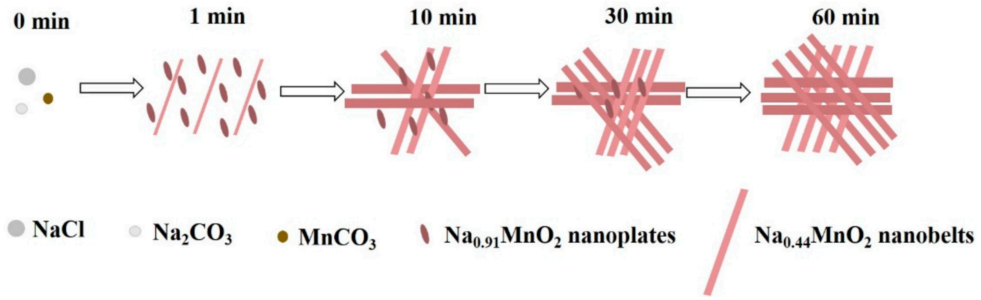

Figure 12. Proposed growth mechanism of $Na_{0.44}MnO_2$ nanobelts.

4. Conclusions

In summary, Li_2MnO_3 nanobelts were prepared via the molten salt method with $Na_{0.44}MnO_2$ nanobelts as precursors at different synthesis conditions, characterized by XRD and SEM, and the reduced Li_2MnO_3 samples were tested as cathodes for lithium-ion batteries. When the reaction temperature was 850 °C, $Na_{0.44}MnO_2$ precursor was uniformly distributed with a smaller particle size of 240 nm. The effect of molten salt contents on the crystallinity was not significant; when the molten salt content was adjusted to 25 g, the $Na_{0.44}MnO_2$ precursor showed the smallest particle size of 204 nm. By comparing the electrochemical performances of reduced Li_2MnO_3, the cyclability and ratability of R-LMO-850 are the best when the reaction temperature of the $Na_{0.44}MnO_2$ precursor is 850 °C; when the amount of molten salt in the reaction system is 25 g, the specific capacity, cycle performance, and ratability of the final product are the best. The synthesis temperature of 850 °C and the molten salt amount of 25 g were considered the optimum synthesis conditions for the $Na_{0.44}MnO_2$ precursor. The growth mechanism of nanobelts was investigated by controlling the reaction time of the $Na_{0.44}MnO_2$ nanobelt precursor. The results indicate that $Na_{0.44}MnO_2$ nanobelts are curled from $Na_{0.91}MnO_2$ nanosheets. The growth mechanism has guiding significance for the synthesis of materials with special morphologies using the molten salt method. These findings are expected to provide a feasible approach for preparing special morphology cathodes for LIBs.

Author Contributions: Conceptualization, J.C.; Methodology, Z.T.; Investigation, M.C.; Resources, Q.H.; Data curation, C.W.; Writing—original draft, Y.S.; Project administration, J.Y. All authors have read and agreed to the published version of the manuscript.

Funding: This research was funded by the Research and Innovation Initiatives of WHPU (No. 2023Y26), the Key Research and Development Project of Hubei Province (No. 2020BBB068) and the Nature Science Foundation of Hubei Province (No. 2020CFB400).

Data Availability Statement: Data are contained within the article.

Conflicts of Interest: The authors declare that they have no competing financial interests or personal relationships that could appear to have influenced the work reported in this paper.

References

1. Yang, Y.; Okonkwo, E.G.; Huang, G.Y.; Xu, S.M.; Sun, W.; He, Y.H. On the sustainability of lithium ion battery industry—A review and perspective. *Energy Storage Mater.* **2021**, *36*, 186–212. [CrossRef]
2. Neumann, J.; Petranikova, M.; Meeus, M.; Gamarra, J.D.; Younesi, R.; Winter, M.; Nowak, S. Recycling of lithium-ion batteries-current state of the art, circular economy, and next generation recycling. *Adv. Energy Mater.* **2022**, *12*, 2102917. [CrossRef]
3. Ding, D.; Li, Z.; Yu, S.; Yang, B.; Yin, Y.; Zan, L.; Myung, N.S. Piezo-photocatalytic flexible PAN/TiO_2 composite nanofibers for environmental remediation. *Sci. Total Environ.* **2022**, *824*, 153790. [CrossRef] [PubMed]
4. Li, K.; Zhou, W.; Li, X.; Li, Q.; Carabineiro, S.A.C.; Fan, J.; Lv, K. Synergistic effect of cyano defects and $CaCO_3$ in graphitic carbon nitridenanosheets for efficient visible-light-driven photocatalytic NO removal. *J. Hazard. Mater.* **2022**, *442*, 130040. [CrossRef] [PubMed]
5. Tian, Y.S.; Zeng, G.B.; Rutt, A.; Shi, T.; Kim, H.; Wang, J.Y.; Koettgen, J.; Sun, Y.Z.; Ouyang, B.; Chen, T.N.; et al. Promises and challenges of next-generation "Beyond Li-ion" batteries for electric vehicles and grid decarbonization. *Chem. Rev.* **2021**, *121*, 1623–1669. [CrossRef]
6. Duffner, F.; Kronemeyer, N.; Tubke, J.; Leker, J.; Winter, M.; Schmuch, R. Post-lithium-ion battery cell production and its compatibility with lithium-ion cell production infrastructure. *Nat. Energy* **2021**, *6*, 123–134. [CrossRef]
7. Harper, G.; Sommerville, R.; Kendrick, E.; Driscoll, L.; Slater, P.; Stolkin, R.; Walton, A.; Christensen, P.; Heidrich, O.; Lambert, S.; et al. Recycling lithium-ion batteries from electric vehicles. *Nature* **2019**, *575*, 75–86. [CrossRef]
8. Manthiram, A. A reflection on lithium-ion battery cathode chemistry. *Nat. Commun.* **2020**, *11*, 1550. [CrossRef]
9. Weiss, M.; Ruess, R.; Kasnatscheew, J.; Levartovsky, Y.; Levy, N.R.; Minnmann, P.; Stolz, L.; Waldmann, T.; Wohlfahrt-Mehrens, M.; Aurbach, D.; et al. Fast Charging of lithium-ion batteries: A review of materials aspects. *Adv. Energy Mater.* **2021**, *11*, 2101126. [CrossRef]
10. Lee, W.; Muhammad, S.; Sergey, C.; Lee, H.; Yoon, J.; Kang, Y.M.; Yoon, W.S. Advances in the cathode materials for lithium rechargeable batteries. *Angew. Chem.-Int. Ed.* **2020**, *59*, 2578–2605. [CrossRef]
11. Nayak, P.K.; Erickson, E.M.; Schipper, F.; Penki, T.R.; Munichandraiah, N.; Adelhelm, P.; Sclar, H.; Amalraj, F.; Markovsky, B.; Aurbach, D. Review on challenges and recent advances in the electrochemical performance of high capacity Li- and Mn-rich cathode materials for Li-ion batteries. *Adv. Energy Mater.* **2018**, *8*, 1702397. [CrossRef]
12. Hu, S.J.; Pillai, A.S.; Liang, G.M.; Pang, W.K.; Wang, H.Q.; Li, Q.Y.; Guo, Z.P. Li-rich layered oxides and their practical challenges: Recent progress and perspectives. *Electrochem. Energy Rev.* **2019**, *2*, 277–311. [CrossRef]
13. Zhao, S.Q.; Guo, Z.Q.; Yan, K.; Wan, S.W.; He, F.R.; Sun, B.; Wang, G.X. Towards high-energy-density lithium-ion batteries: Strategies for developing high-capacity lithium-rich cathode materials. *Energy Storage Mater.* **2021**, *34*, 716–734. [CrossRef]
14. Yin, C.; Wei, Z.N.; Zhang, M.H.; Qiu, B.; Zhou, Y.H.; Xiao, Y.G.; Zhou, D.; Yun, L.; Li, C.; Gu, Q.W.; et al. Structural insights into composition design of Li-rich layered cathode materials for high-energy rechargeable battery. *Mater. Today* **2021**, *51*, 15–26. [CrossRef]
15. Mabokela, T.E.; Nwanya, A.C.; Ndipingwi, M.M.; Kaba, S.; Ekwere, P.; Werry, S.T.; Ikpo, C.O.; Modibane, K.D.; Iwuoha, E.I. Review—Recent advances on high-capacity Li-rich layered manganese oxide cathodes. *J. Electrochem. Soc.* **2021**, *168*, 070530. [CrossRef]
16. Tran, N.; Croguennec, L.; Menetrier, M.; Weill, F.; Biensan, P.; Jordy, C.; Delmas, C. Mechanisms associated with the "Plateau" observed at high voltage for the overlithiated $Li_{1.12}(Ni_{0.425}Mn_{0.425}Co_{0.15})_{0.88}O_2$ system. *Chem. Mater.* **2008**, *20*, 4815–4825. [CrossRef]
17. Phillips, P.J.; Bareno, J.; Li, Y.; Abraham, D.P.; Klie, R.F. On the localized nature of the structural transformations of Li_2MnO_3 following electrochemical cycling. *Adv. Energy Mater.* **2015**, *5*, 1501252. [CrossRef]
18. Oishi, M.; Yamanaka, K.; Watanabe, I.; Shimoda, K.; Matsunaga, T.; Arai, H.; Ukyo, Y.; Uchimoto, Y.; Ogumi, Z.; Ohta, T. Direct observation of reversible oxygen anion redox reaction in Li-rich manganese oxide, Li_2MnO_3, studied by soft X-ray absorption spectroscopy. *J. Mater. Chem. A* **2016**, *4*, 9293–9302. [CrossRef]
19. Chen, H.R.; Islam, M.S. Lithium extraction mechanism in Li-rich Li_2MnO_3 involving oxygen hole formation and dimerization. *Chem. Mater.* **2016**, *28*, 6656–6663. [CrossRef]

20. Ma, J.; Zhou, Y.N.; Gao, Y.R.; Kong, Q.Y.; Wang, Z.X.; Yang, X.Q.; Chen, L.Q. Molybdenum substitution for improving the charge compensation and activity of Li_2MnO_3. *Chem. A Eur. J.* **2014**, *20*, 8723–8730. [CrossRef]
21. Dong, X.; Xu, Y.L.; Xiong, L.L.; Sun, X.F.; Zhang, Z.W. Sodium substitution for partial lithium to significantly enhance the cycling stability of Li_2MnO_3 cathode material. *J. Power Sources* **2013**, *243*, 78–87. [CrossRef]
22. Gao, Y.R.; Wang, X.F.; Ma, J.; Wang, Z.X.; Chen, L.Q. Selecting substituent elements for Li-rich Mn-based cathode materials by Density Functional Theory (DFT) Calculations. *Chem. Mater.* **2015**, *27*, 3456–3461. [CrossRef]
23. He, H.B.; Cong, H.J.; Sun, Y.; Zan, L.; Zhang, Y.X. Spinel-layered integrate structured nanorods with both high capacity and superior high-rate capability as cathode material for lithium-ion batteries. *Nano Res.* **2017**, *10*, 556–569. [CrossRef]
24. Wu, F.; Li, N.; Su, Y.F.; Zhan, L.J.; Bao, L.Y.; Wang, J.; Chen, L.; Zheng, Y.; Dai, L.Q.; Peng, J.Y.; et al. Ultrathin spinel membrane-encapsulated layered lithium-rich cathode material for advanced Li-ion batteries. *Nano Lett.* **2014**, *14*, 3550–3555. [CrossRef] [PubMed]
25. Liu, H.; Du, C.Y.; Yin, G.P.; Song, B.; Zuo, P.J.; Cheng, X.Q.; Maa, Y.L.; Gao, Y.Z. An Li-rich oxide cathode material with mosaic spinel grain and a surface coating for high performance Li-ion batteries. *J. Mater. Chem. A* **2014**, *2*, 15640–15646. [CrossRef]
26. Kubota, K.; Kaneko, T.; Hirayama, M.; Yonemura, M.; Imanari, Y.; Nakane, K.; Kanno, R. Direct synthesis of oxygen-deficient $Li_2MnO_{3\text{-}x}$ for high capacity lithium battery electrodes. *J. Power Sources* **2012**, *216*, 249–255. [CrossRef]
27. Sun, Y.; Cong, H.J.; Zang, L.; Zhang, Y.X. Oxygen vacancies and stacking faults introduced by low-temperature reduction improve the electrochemical properties of Li_2MnO_3 nanobelts as lithium-ion battery cathodes. *ACS Appl. Mater. Interfaces* **2017**, *9*, 38545–38555. [CrossRef]
28. Sun, Y.; Zan, L.; Zhang, Y.X. Enhanced electrochemical performances of Li_2MnO_3 cathode materials via adjusting oxygen vacancies content for lithium-ion batteries. *Appl. Surf. Sci.* **2019**, *483*, 270–277. [CrossRef]
29. Sun, Y.; Guo, M.H.; Shu, S.W.; Ding, D.; Wang, C.L.; Zhang, Y.X.; Yan, J.T. Preparation of Li_2MnO_3 nanowires with structural defects as high rate and high capacity cathodes for lithium-ion batteries. *Appl. Surf. Sci.* **2022**, *585*, 152605. [CrossRef]
30. Wang, C.C.; Jarvis, K.A.; Ferreira, P.J.; Manthiram, A. Effects of synthesis conditions on the first charge and reversible capacities of lithium-rich layered oxide cathodes. *Chem. Mater.* **2013**, *25*, 3267–3275. [CrossRef]
31. Chen, Y.; Chen, Z.; Xie, K. Effect of annealing on the first-cycle performance and reversible capabilities of lithium-rich layered oxide cathodes. *J. Phys. Chem. C* **2014**, *118*, 11505–11511. [CrossRef]
32. Wang, Y.; Li, H.; He, P.; Hosono, E.; Zhou, H. Nano active materials for lithium-ion batteries. *Nanoscale* **2010**, *2*, 1294–1305. [CrossRef] [PubMed]
33. Wang, K.X.; Li, X.H.; Chen, J.S. Surface and interface engineering of electrode materials for lithium-on batteries. *Adv. Mater.* **2015**, *27*, 527–545. [CrossRef] [PubMed]
34. Kim, D.K.; Muralidharan, P.; Lee, H.-W.; Ruffo, R.; Yang, Y.; Chan, C.K.; Peng, H.; Huggins, R.A.; Cui, Y. Spinel $LiMn_2O_4$ nanorods as lithium ion battery cathodes. *Nano Lett.* **2010**, *10*, 3852–3856. [CrossRef] [PubMed]
35. Zhang, X.; Tang, S.; Du, Y. Synthesis, characterization, and exchange bias effect in single crystalline $Li_{0.44}MnO_2$ nanoribbons. *J. Phys. Chem. C* **2011**, *115*, 2644–2649. [CrossRef]
36. Hosono, E.; Matsuda, H.; Saito, T.; Kudo, T.; Ichihara, M.; Honma, I.; Zhou, H. Synthesis of single crystalline $Li_{0.44}MnO_2$ nanowires with large specific capacity and good high current density property for a positive electrode of Li ion battery. *J. Power Sources* **2010**, *195*, 7098–7101. [CrossRef]
37. Yang, J.R.; Weng, W.; Xiao, W. Electrochemical synthesis of ammonia in molten salts. *J. Energy Chem.* **2020**, *43*, 195–207. [CrossRef]
38. Tan, W.D.; Guo, X.S.; She, Y.M.; Li, H.S.; Lei, Y.; You, J.G.; Zhang, X.F.; Luo, X.D. Effects of molten salt temperature and holding time on synthesis of hercynite by molten salt method. *Ceram. Int.* **2022**, *48*, 11555–11560. [CrossRef]
39. Lee, J.S. Preparation of $EuAlO_3$ powders by molten salt method. *J. Ceram. Process. Res.* **2017**, *18*, 385–388.
40. Zhang, X.; Tang, S.; Du, Y. Controlled synthesis of single-crystalline $Li_{0.44}MnO_2$ and Li_2MnO_3. *Mater. Res. Bull.* **2012**, *47*, 1636–1640. [CrossRef]
41. Zhao, N.N.; Li, Y.S.; Zhao, X.X.; Zhi, X.K.; Liang, G.C. Effect of particle size and purity on the low temperature electrochemical performance of $LiFePO_4$/C cathode material. *J. Alloys Compd.* **2016**, *683*, 123–132. [CrossRef]
42. Thackeray, M.M.; Kang, S.H.; Johnson, C.S.; Vaughey, J.T.; Benedek, R.; Hackney, S.A. Li_2MnO_3-stabilized $LiMO_2$ (M = Mn, Ni, Co) electrodes for lithium-ion batteries. *J. Mater. Chem.* **2007**, *17*, 3112–3125. [CrossRef]
43. Xiao, L.; Xiao, J.; Yu, X.; Yan, P.; Zheng, J.; Engelhard, M.; Zhang, J.G. Effects of structural defects on the electrochemical activation of Li_2MnO_3. *Nano Energy* **2015**, *16*, 143–151. [CrossRef]
44. Hwang, I.; Lee, C.W.; Kim, J.C.; Yoon, S. Particle size effect of Ni-rich cathode materials on lithium ion battery performance. *Mater. Res. Bull.* **2012**, *47*, 73–78. [CrossRef]
45. Drezen, T.; Kwon, N.H.; Bowen, P.; Teerlinck, I.; Isono, M.; Exnar, I. Effect of particle size on $LiMnPO_4$ cathodes. *J. Power Sources* **2007**, *174*, 949–953. [CrossRef]
46. Chu, Q.X.; Wang, X.F.; Li, B.X.; Jin, H.; Cao, X.J.; Zhao, X.D.; Liu, X.Y. Flux synthesis and growth mechanism of $Na_{0.5}MnO_2$ whiskers. *J. Cryst. Growth* **2011**, *322*, 103–108. [CrossRef]
47. Wang, X.; Li, Y.D. Rare-earth-compound nanowires, nanotubes, and fullerene-like nanoparticles: Synthesis, characterization, and properties. *Chem. A Eur. J.* **2003**, *9*, 5627–5635. [CrossRef] [PubMed]
48. Li, Y.G.; Wu, Y.Y. Formation of $Na_{0.44}MnO_2$ nanowires via stress-induced splitting of birnessite nanosheets. *Nano Res.* **2009**, *2*, 54–60. [CrossRef]

49. Zhang, Z.R.; Wang, Z.N.; He, S.N.; Wang, C.Q.; Jin, M.S.; Yin, Y.D. Redox reaction induced Ostwald ripening for size- and shape-focusing of palladium nanocrystals. *Chem. Sci.* **2015**, *6*, 5197–5203. [CrossRef] [PubMed]
50. Johnson, N.J.J.; Korinek, A.; Dong, C.H.; van Veggel, F. Self-focusing by Ostwald ripening: A strategy for layer-by-layer epitaxial growth on upconverting nanocrystals. *J. Am. Chem. Soc.* **2012**, *134*, 11068–11071. [CrossRef]